# Interfacing Electrogenic Cells with 3D Nanoelectrodes: Position, Shape, and Size Matter

**Francesca Santoro,[†] Sabyasachi Dasgupta,[‡] Jan Schnitker,[†] Thorsten Auth,[‡] Elmar Neumann,[†] Gregory Panaitov,[†] Gerhard Gompper,[‡] and Andreas Offenhäusser[†,*]**

[†]Institute of Bioelectronics (ICS-8/PGI-8) and [‡]Institute of Theoretical Soft Matter and Biophysics (ICS-2/IAS-2), Forschungszentrum Jülich, 52428 Jülich, Germany

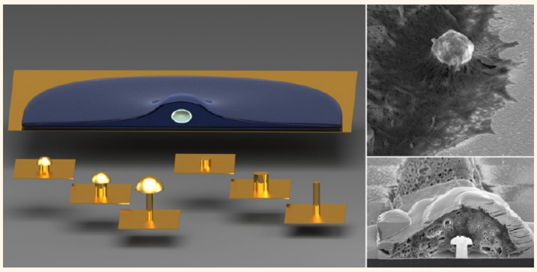

**ABSTRACT** An in-depth understanding of the interface between cells and nanostructures is one of the key challenges for coupling electrically excitable cells and electronic devices. Recently, various 3D nanostructures have been introduced to stimulate and record electrical signals emanating from inside of the cell. Even though such approaches are highly sensitive and scalable, it remains an open question how cells couple to 3D structures, in particular how the engulfment-like processes of nanostructures work. Here, we present a profound study of the cell interface with two widely used nanostructure types, cylindrical pillars with and without a cap. While basic functionality was shown for these approaches before, a systematic investigation linking experimental data with membrane properties was not presented so far. The combination of electron microscopy investigations with a theoretical membrane deformation model allows us to predict the optimal shape and dimensions of 3D nanostructures for cell-chip coupling.

**KEYWORDS:** 3D nanoelectrodes · electrogenic cells · cell—nanostructure interface · membrane deformation · engulfment-like mechanism · focused ion beam · scanning electron microscopy

Several techniques for interfacing excitable cells with electrical devices have been developed to study ion channel functionality over the long-term,[1] restore lost sensing capabilities,[2] control motor disorders,[3] and control heartbeat.[4] The success of the numerous extracellular interface concepts proposed in basic science is limited by problems ranging from improper cell adhesion to inadequate device stability.[5] To overcome such limitations, the design of engineered interfaces[6,7] is mainly based on successful application of emerging technologies, such as nanotechnology.[8−11] The interface between cells and nanostructures has been studied extensively.[12−16] In particular, the morphology of cells interfacing 3D nanoelectrodes has been investigated in detail,[17−27] as these are prominent candidates to solve the aforementioned problems. Potential mechanisms for coupling between electrogenic cells and multiple 3D nano- and microstructures are proposed and used for extracellular applications.[6,9,10,26,28−32] Most of these 3D nano- and microstructures can be classified under two main types: cylindrical pillars with and without a cap. Here, the cell response depends on the cytoskeletal contribution driven by an actin ring, which forms around the 3D nanostructures,[33] enabling the engulfment-like event.[34−36] Former studies lack information about how a cell interfaces a single 3D nanostructure, which is the basic investigation needed for understanding the cell interaction with multiple 3D nanostructures. Moreover, several important and fundamental questions were not addressed yet. Which of the two most-used structures leads to a better engulfment-like event by the cell? How does the position of the engulfment-like event affect the cell response and the coupling to the 3D nanostructure? Here, we present a methodical investigation of the cell-3D nanostructure interface using focused ion beam (FIB) and scanning electron microscopy (SEM). We characterize the position of the engulfment-like event of 3D nanopillars by cardiomyocyte-like HL-1 cells[37] and the deformation of the extracellular membrane. Finally, we investigate which 3D nanoelectrodes are optimal for engulfment by cardiomyocyte-like cells to find the best design in

* Address correspondence to a.offenhaeusser@fz-juelich.de.

Received for review January 21, 2014 and accepted June 25, 2014.

10.1021/nn500393p

terms of dimension and shape, and explain the biological driving forces that favor one structure over the other. This work will facilitate a prediction of the optimal parameter combination for the best coupling of electrogenic cells with 3D nanoelectrodes for *in vitro* and *in vivo* applications.

## RESULTS AND DISCUSSION

**HL-1 Cells on 3D Nanostructures: Position of the Engulfment-like Event.** First, we analyzed the location of the engulfment-like event as schematically shown in Figure 1a. It is known that during a typical endocytic event, the cell membrane wraps around the particle that is then internalized by a cell.[38,39] We investigated the relative position of an engulfment-like event by an electrogenic cell type (HL-1 cells) on cylindrical nanopillars with and without mushroom-shaped caps. We fabricated nanostructure arrays with a pitch of 25 $\mu$m, to ensure that in most cases a cell adheres only to a single 3D nanostructure. We tested nanopillars with stalk height, $H$, from 300 up to 1000 nm and radius, $R_s$, from 150 to 400 nm (examples are given in Figure 1b, i–vi), with aspect ratio, $\gamma$ ($H/2R_s$), of the stalk in the range of 0.4–3.3 (see Supporting Information S1). For cylinders with caps, we considered a cap radius, $R_c$, that varied in the range of 300–1000 nm. HL-1 cells[37] were cultured on 3D nanostructures for 3 days *in vitro* (DIV) and then chemically fixed. The membrane and the nucleus were fluorescently stained. The cells were observed with fluorescent microscopy (Figure 1c, i–iv)

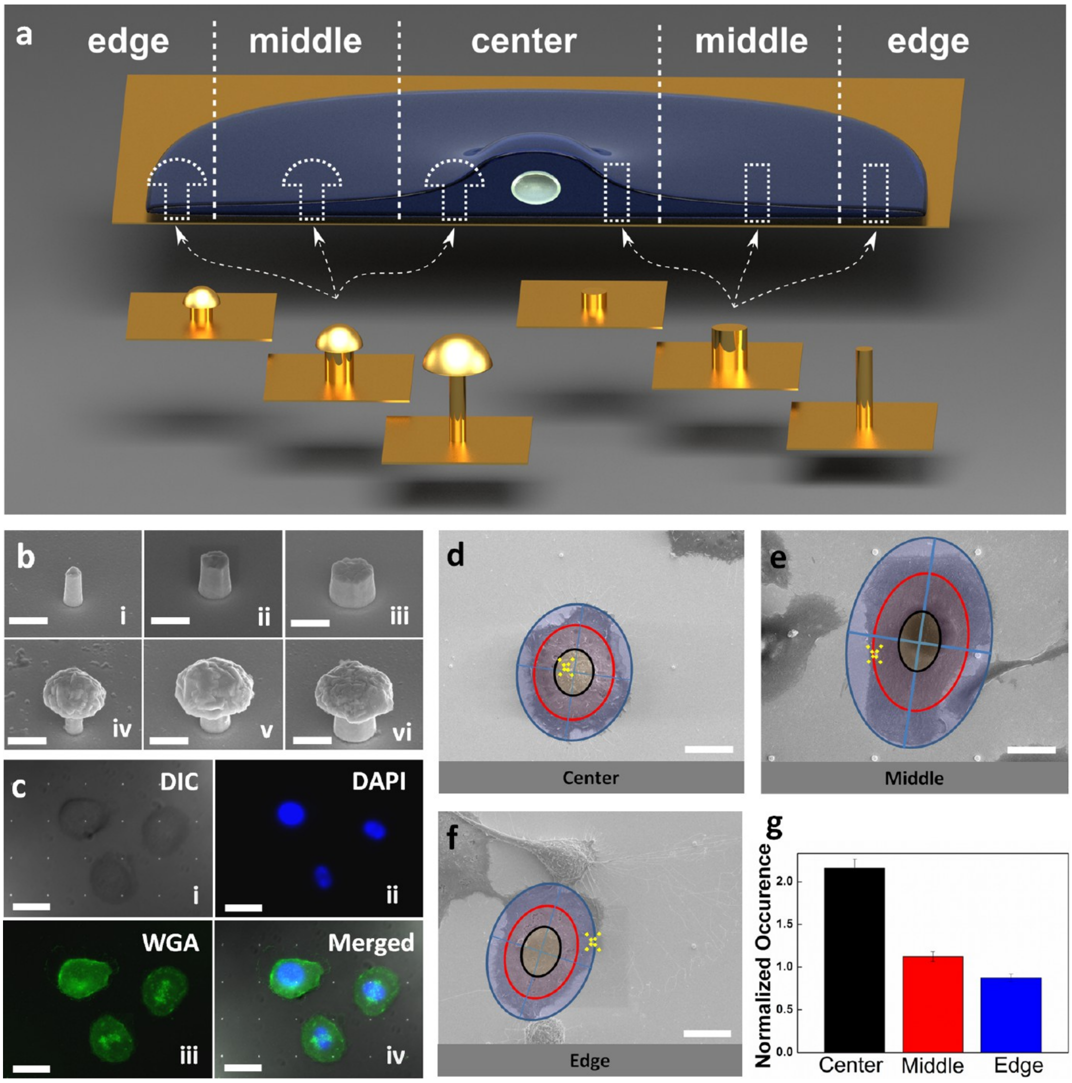

Figure 1. Investigation of engulfment-like events of HL-1 cells on 3D nanostructures. (a) schematic for the position of the engulfment-like event in the cell on cylinders with and without caps (different stalk aspect ratios); (b) example of nanostructured gold cylinders without caps (i–iii) and cylinders with caps (iv–vi) on planar gold (scale bar 0.8 $\mu$m, tilt 52°); (c) DIC image of HL-1 cells on an array of 3D nanostructures (i) HL-1 nuclei stained with DAPI in blue (ii), wheat germ agglutinin (WGA) staining of the cell membrane in green (iii) and merged DIC, DAPI, and WGA image (iv) (scale bar 25 $\mu$m); (d) scanning electron micrograph (SEM) of an HL-1 cell engulfing a 3D nanostructure in the center; (e) in the middle; (f) at edge of the cell (yellow cross indicates the position of the pillar, scale bars 15 $\mu$m); (g) normalized occurrence of engulfment events in the center, middle, and edge of the cell.

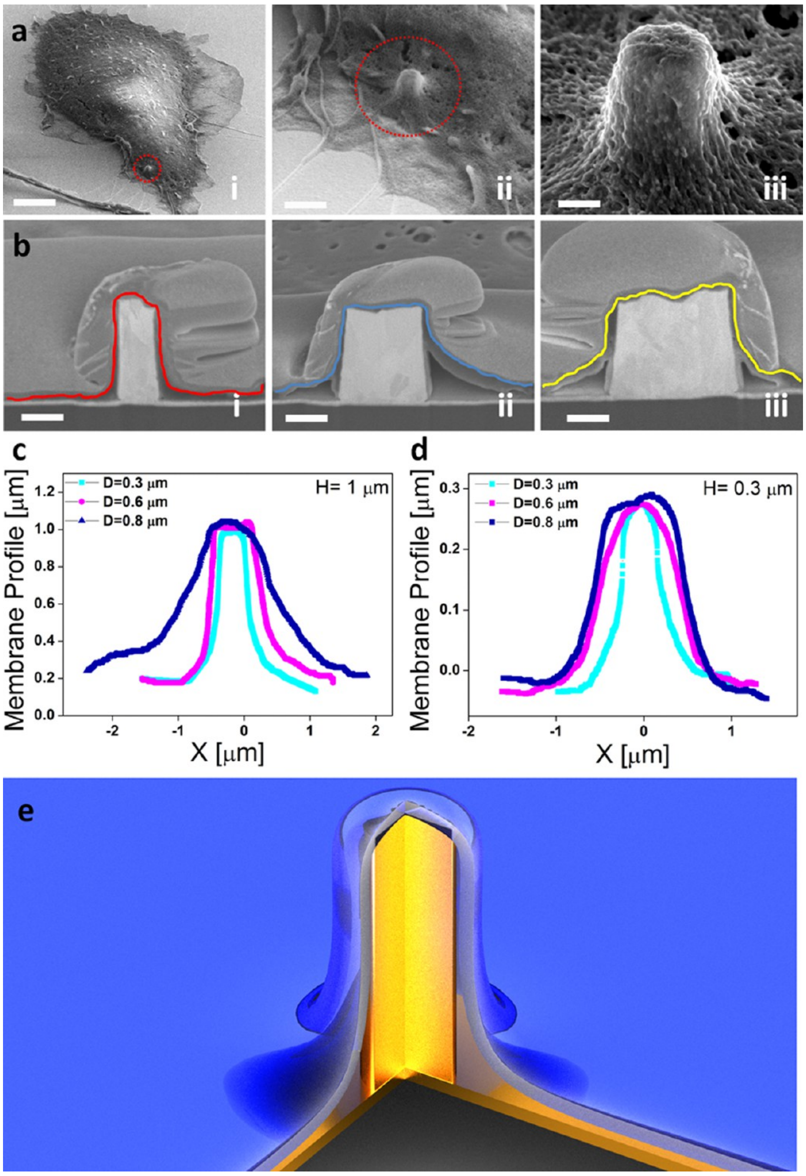

**Figure 2. Free membrane deformation at the edge of the cell as response to 3D cylindrical nanostructures without caps. (a) SEM micrographs of individual fixed HL-1 cells, each engulfing a cylinder without a cap ((i) scale bar 10 $\mu$m, (ii) scale bar 1 $\mu$m, (iii) scale bar 0.2 $\mu$m); (b) FIB cross sections of fixed HL-1 on cylinders without caps (scale bars 0.3 $\mu$m); (c) membrane profiles for different diameter pillars with cylinder height of 1 $\mu$m; (d) membrane profiles for different diameter pillars with cylinder height of 0.3 $\mu$m; (e) schematic of a cell promoting an engulfment-like event of a cylindrical nanopillar without cap at the edge of the cell.**

and SEM after critical point drying. To quantify the relative position of a single 3D nanostructure, the cell shape was fit with three equidistant and concentric elliptical regions of interest (ROIs) with respect to the ellipse axes (Figure 1d–f). The blue ROI determines the edge of cell, the red ROI defines the middle of the cell and the black ROI represents the center of the cell, where the nucleus was located in most cases. We found 23% of engulfment-like events in the center, 37% in the middle and 40% at the edge of the cell. When normalizing the rate to the effective area, we find double the occurrence of structures in the center of the compared to the middle and at the edge of the cell (Figure 1g).

**Nanostructures Engulfed at the Edge of the Cell Favor Engulfment and Free Membrane Deformation.** Next, we studied engulfment-like events at the edge of the cell in more detail. From our SEM investigation, we observed cells deforming their cell membrane according to the shape of the nanopillar (Figure 2a, 3a). To further characterize the interface between the cell membrane and the 3D nanopillars, we performed sequential cross sectioning (see Supporting Information S2) of cells ($N = 110$) with FIB and acquired images with SEM. The junctional membrane detaches from the planar substrate revealing the rough planar gold, which was further analyzed by atomic force microscopy (AFM) measurements (see Supporting Information S5).

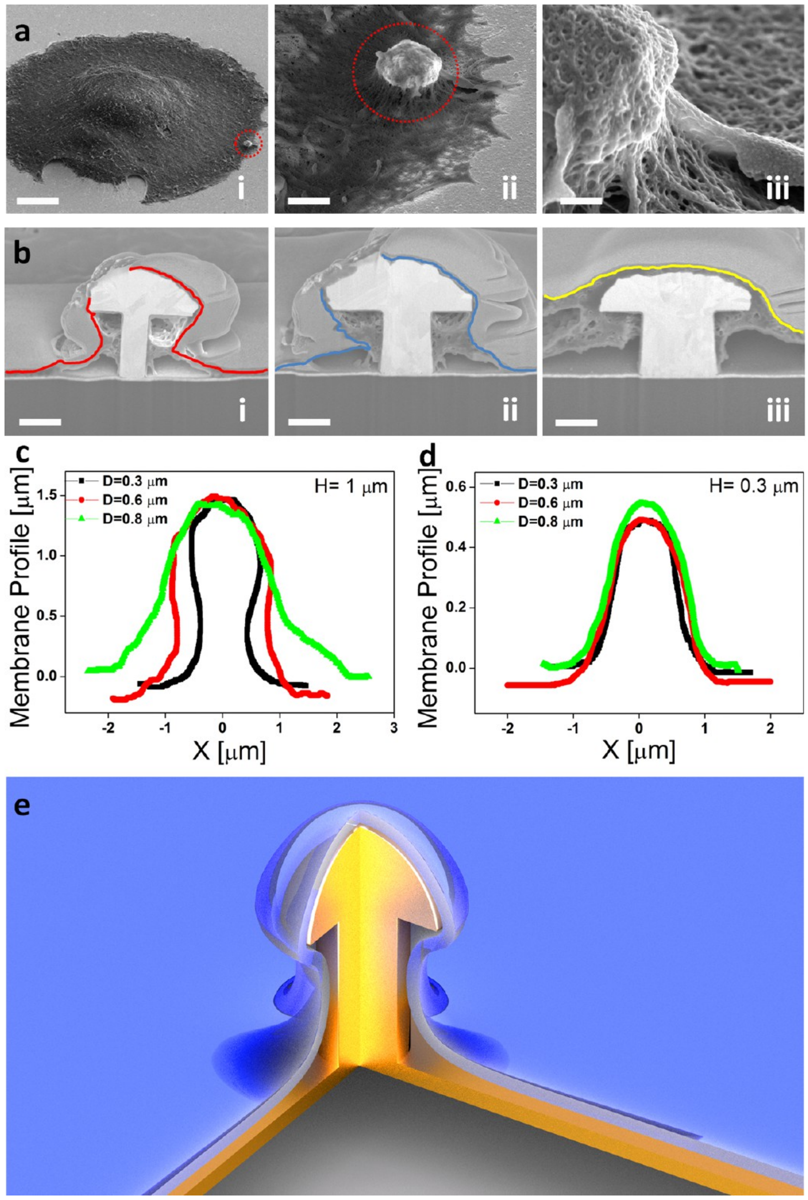

**Figure 3. Free membrane deformation at the edge of the cell as response to 3D cylindrical nanostructures with caps. (a) SEM micrographs of individual fixed HL-1 cells engulfing a cylinder with a cap ((i) scale bar 5 $\mu$m, (ii) scale bar 1.5 $\mu$m, (iii) scale bar 250 nm); (b) FIB cross sections of fixed HL-1 on cylinders with caps (scale bars 0.3 $\mu$m); (c) membrane profiles for different stalk diameters with stalk height 1 $\mu$m; (d) membrane profiles for different stalk diameter pillars with cylinder height of 0.3 $\mu$m; (e) schematic of a cell promoting an engulfment-like event of a cylindrical nanopillar with cap at the edge of the cell.**

We refer to the extracellular membrane domain facing the substrate as "junctional" membrane, and the domain facing the culture medium as "free" membrane as previously established in literature.[40] Analyzing the cross sections through the center of the nanopillar, we trace the shape of the free membrane (solid line) as in Figure 2b, Figure 3b. At the cell edge, we found that the junctional membrane adheres around the nanopillar for all shapes and dimensions and also remains attached to the surrounding flat gold substrate while the free membrane develops different shapes. For a detailed study of the free membrane response to nanopillars with different dimensions and shapes, we plot the membrane shapes for different $H$ and $R_s$, as shown in Figure 2c,d and Figure 3c,d. Cylinders without caps favor a "tent-like" deformation of the free membrane (Figure 2c,d) independent of the actual cylinder dimensions. Independent of $R_s$, tent-like deformations were observed only around cylinders with caps only in the case of small $H$ (and thus low $\gamma$), as shown in Figure 3d. High pillars with caps promote an hourglass shape, in particular for the smallest $R_s$ (150 nm) as shown in Figure 3c with $\gamma = 3.3$. From our experimental investigation, we could distinguish two elementary scenarios: hourglass-like membrane shapes, as induced by taller capped cylinders (Figure 3e), and tent-like shapes, as induced by cylinders without caps (Figure 2e) or small capped cylinders. These two

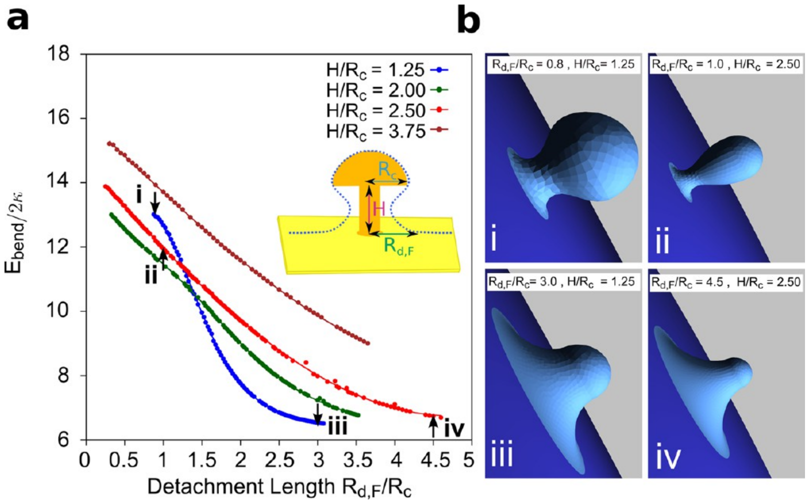

**Figure 4. Theoretical analysis of the membrane deformation profiles at the edge of the cell. (a) Bending energy for different stalk heights, $H$, and cap radii, $R_c$, as a function of the detachment length, $R_{d,F}/R_c$. Because of the scale invariance, the bending energy depends only on the ratios $H/R_c$ and $R_{d,F}/R_c$ and not on the absolute values of the dimensions. (b) Membrane shapes for the parameter values indicated by the arrows in the inset of (a).**

scenarios can be better understood by analyzing the FIB/SEM micrographs in Figure 2b and Figure 3b, where we observe that the intracellular region is very thin because of the nearly 2D structure of the cytoskeleton[41] at the edge of the cell. Motivated by the experimental observations described above, we construct a theoretical model to investigate the role of capped pillar height by neglecting the cytoskeletal contribution, and estimating the deformation energy by a continuum curvature-elasticity Helfrich description of the membrane.[42] We considered a semispherical cap of radius $R_c$ placed at height $H$ above the planar substrate. The free membrane wraps around the cap and flattens onto the planar substrate at detachment length, $R_{d,F}$, closely paralleling the junctional membrane, with only a thin layer of intracellular material. To investigate how the pillar height influences the free membrane response, we define the ratio $H/R_c$ as a fundamental parameter. We assume that the membrane has a bending rigidity, $\kappa$, which expresses the resistance of the membrane to bending deformations. A final parameter is $R_{d,F}/R_c$, which indicates the cell's response to the planar substrate *vs* the width of the cap. We use $\kappa = 50k_BT$ (resulting in a Young's modulus $E \sim 10^6{-}10^7$ Pa for a thin membrane sheet), as previously shown for red blood cells.[43] We evaluate the free membrane's shape at equilibrium by calculating the deformation energy for several values of $H/R_c$ as a function of the detachment length, *i.e.*, as a function of $R_{d,F}/R_c$. Hourglass membrane shapes occur only at intermediate $H/R_c$ (*i.e.*, 2 and 2.5) and only when $R_{d,F}/R_c$ is small. In these cases, the deformation energy is smaller than that for low or high $H/R_c$ with small $R_{d,F}/R_c$ (Figure 4a). However, the hourglass membrane profiles (states (i) and (ii) in Figure 4) for small $R_{d,F}/R_c$ require higher deformation energy costs $E_{bend}$ than tent-like shapes with large $R_{d,F}/R_c$ (states (iii) and (iv) in Figure 4 (see also Supporting Information S8). An effective contact interaction of the free membrane can be characterized by the adhesion strength $w$ which can be extracted from the local mean curvature of the free membrane at the detachment point (see Supporting Information S8). In our experiments, we utilized caps with an average radius of 400 nm, and $H/R_c = 1.25$ or $H/R_c = 2.5$ that correspond to stalk heights of 0.5 and 1 $\mu$m, respectively. We calculate the membrane deformation profiles for structures of these two heights for different detachment lengths (see Supporting Information S8). As expected from the deformation energy calculations, hourglass deformations are found for these favorable nanopillar heights (Figure 3c), while the shorter pillars, as in Figure 3d are wrapped less. Figures 3c and 3d illustrate that the membrane deformation scales with stalk radius, $R_s$, for cylindrical pillars, as expected for systems dominated by bending rigidity. However, the higher bending-energy costs for the hourglass states compared to the tent-like states need to be compensated; we believe that this is achieved by the actin of the free membrane joining toward the junctional membrane (Figure 3b) thereby providing higher effective contact interaction.

**Nanopillar Shape and Dimension Induce Differences in Junctional Membrane Deformation at the Cell Center.** Finally, we investigated the interface of HL-1 cells on 3D nanostructures when an engulfment-like event occurs at the center of the cell. We observed that the free membrane does not sense the structure underneath, which allows us to focus on the interaction of the 3D nanostructure with the junctional membrane. During the endocytosis of a nanoparticle, the actin filaments provide key active forces during membrane wrapping.[34−36] In the case of 3D nanostructures fixed on a substrate, the membrane

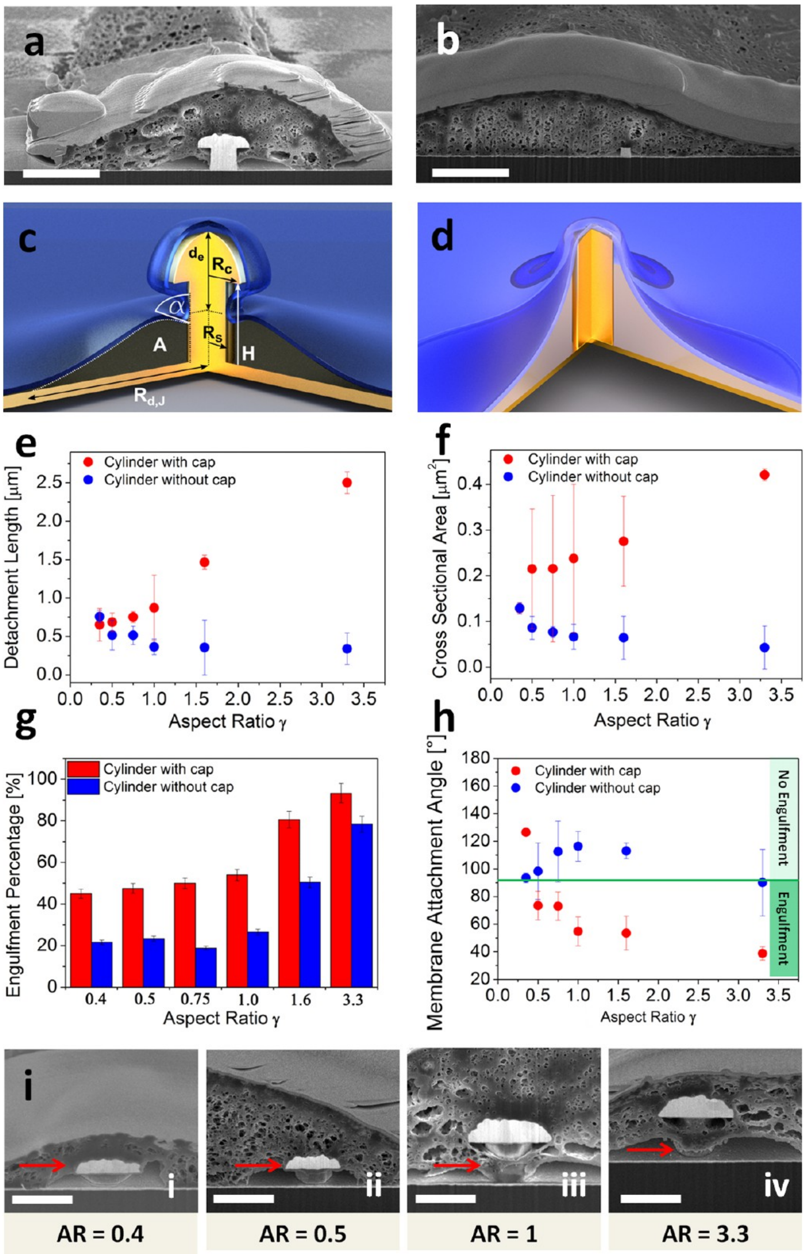

**Figure 5. Junctional membrane deformation investigation in the center of the cell. (a) FIB cross section of HL-1 engulfing a cylinder with a cap in the center of the cell (scale bar 1 $\mu$m); (b) FIB cross section of HL-1 engulfing a cylinder without a cap in the center of the cell (scale bar 1 $\mu$m); (c) schematic of experimental parameters calculated for cylinders with caps and (d) schematic of junctional membrane attaching a cylinder without cap; (e) junctional membrane detachment length, $R_{d,J}$, plotted as a function of the stalk aspect ratio, $\gamma$; (f) area, *A*, plotted as a function of $\gamma$; (g) engulfment percentage, *f*, plotted as a function of $\gamma$; (h) angle, $\alpha$, plotted as a function of $\gamma$, with the engulfment threshold at 90°; (i) ring like structure on the stalk at different values of $\gamma$ (I and ii scale bar, 1 $\mu$m; iii and iv scale bar, 1.5 $\mu$m).**

does not form a complete bud encapsulating the structure, but the junctional membrane deforms and establishes a ring-like assembly around the 3D structure.[33] In the center of the cell, the central junctional membrane only partially attaches to the pillar, and detaches from the flat gold surface of the substrate (Figure 5a,b). These phenomena were previously observed for Neuro-2a[18] and primary neurons,[44] where the membrane engulfing a mushroom-like nanostructure in the center of the cell detached from the planar substrate. We investigated the junctional membrane responses to the 3D nanostructures by analyzing FIB cross sections through the center of the pillar (Figure 5a,b). The junctional membrane was characterized with regard to four independent parameters as shown in Figure 5c,d (see also Supporting Information S2). These parameters are the detachment length of the junctional membrane ($R_{d,J}$), the cross-sectional area of the detaching membrane (*A*), the engulfment length ($d_e$), and the attachment angle ($\alpha$). $R_{d,J}$ is the horizontal distance from the membrane attachment point on the planar substrate to the central *z*-axis of the pillar.

$d_e$ is evaluated as the vertical projection from the top of the pillar to the membrane attaching point on the pillar stalk, as shown in Figure 5c. α is the angle between the curving membrane and the vertical of the pillar, at the point where the membrane is not attached to the stalk under the cap (see Supporting Information S3). On the one hand, for stalk aspect ratios between 0.4 and 0.75, $R_{d,J}$ for the nanopillars with and without cap are comparable (0.75 $\mu$m in average) as shown in Figure 5e. On the other hand, when the aspect ratio is highest (3.3), we observed an average $R_{d,J}$ of 0.25 $\mu$m on for a nanopillar without a cap, while $R_{d,J}$ was more than 10 times higher (2.6 $\mu$m) for a nanopillar with a cap. The difference in $R_{d,J}$ causes the resulting difference in $A$ of 0.42 and 0.04 $\mu m^2$ for a cylinder with a cap and without a cap, respectively (Figure 5f). We calculate the engulfment percentage, *f*, as the ratio between $d_e$ and the total height of the pillar (Figure 5g). For both shapes, the highest engulfment percentage was achieved at the highest aspect ratio ($\gamma = 3.3$). In this case, the cells engulf 75% of the volume of nanopillars without cap and up to 95% of the volume of nanopillars with cap. To analyze α, the tangent of the junctional membrane was extended to the vertical axis of the pillar (see Supporting Information S3). We define a threshold engulfment angle when the membrane forms an angle less than 90° with the vertical axis of the pillar, as shown in Figure 5h and described in details in the Supporting Information S3. According to our data, all nanopillars with caps promote an engulfment-like event, except for structures of the lowest aspect ratio, $\gamma = 0.4$. We assume that the curvature of the junctional membrane is influenced mostly by the cytoskeletal forces pulling the junctional membrane toward the free membrane while the actin ring around the nanopillar is mostly generating forces pulling the junctional membrane toward the substrate.[36] Moreover, we assume that the actin filaments influence the membrane attachment point on the stalk (Figure 5i). At highest aspect ratio (*i.e.*, 3.3), we found the biggest detachment length (and thus the area), the highest engulfment percentage and the smallest attachment angle. The angle, in particular, is a very important parameter since angles lower than 90° indicate that the membrane highly deforms around the 3D nanostructure. In fact, such a high wrapping state is comparable to what happens for complete phagocytosis events where the membrane deforms around the particle until the complete encapsulation. This means that for typical phagocytosis events, the membrane pulls toward the particle to form an invagination. Here, the membrane "tries" to invaginate the 3D nanostructures and deforms accordingly. Since the 3D nanostructure is fixed on the planar substrate, the cell is not able to internalize it but the cell membrane stays in the invaginating deforming status. For angles greater than 90° the membrane has a tent-like deformation, which is clearly a sign for a nonencapsulating–like membrane. On the basis of the calculated parameters, we approximated effective seal resistances in the vicinity of the nanoelectrodes with an assumed constant gap between adhered junctional membrane and the nanoelectrode (see Supporting Information S6).

We analyzed the central membrane deformation profiles theoretically (see Supporting Information S7) by the same model used for the description of the engulfment-like event at the edge of the cell. In addition, we consider the contribution of the cytoskeleton stress, which we quantify by an effective pressure, *p*, normal to the planar substrate. For fixed engulfment percentage and detachment length, we find a transition from a tent-like deformation without cytoskeletal stress, to more curved shape of the junctional membrane at high cytoskeletal stress (Figure 6a, i–iv). The theoretical model is applicable for fitting every experimental data set with good agreement, here we show few examples in Figure 6d–g. This agreement justifies the choice of an effective pressure for the cytoskeleton stress in our model, as schematically shown in Figure 6b. As done previously for the edge of the cell, we assumed a bending rigidity of $\kappa = 50k_BT$ for the junctional membrane. The cytoskeletal stress and adhesion strength of the cell to the substrate are extracted from the averaged experimental data (Figure 6c and inset). The cytoskeletal stress for cylinders without caps is $p < 440$ Pa, which is comparable to cytoskeletal stress reported for fibroblasts[45] (range from 10 Pa to several kPa). Up to $\gamma = 1.6$, the cytoskeletal stress increases with the pillar's aspect ratio. Then it appears to have decreased again at $\gamma = 3.3$. However, the uncertainty for the calculated high cytoskeletal stress is large, as discussed in the Supporting Information S7. Surprisingly, in the case of cylinders with caps, the cytoskeletal stress is 1 order of magnitude smaller than for cylinders without caps for that the cytoskeletal stress is $p < 30$ Pa. This shows that the cell is actively responding to the presence of the nanopillars and that the cytoskeleton adapts to the substrate underneath. This distinguishes our model from the model of Xie *et al.*[27] where the membrane deformation is influenced mostly by gravitational forces. For capped nanopillars with $\gamma = 1.6$ and $\gamma = 3.3$, we find cytoskeletal stresses of only $p < 2$ Pa. This indicates that capped nanopillars with high aspect ratio more easily promote an engulfment-like event by HL-1 cells than all other nanopillars that we have studied. Points of attachment with enriched adhesion molecules have been reported previously on 3D nanostructures.[46] We find for cylinders with and without cap that these regions of presumably higher adhesion strength correspond to areas requiring strong cytoskeletal pulling forces to achieve the membrane deformations observed (inset Figure 6c). We found adhesion strengths between the cell and the substrate of up to $w = 5\ \mu J/m^2$ for cylinders without cap

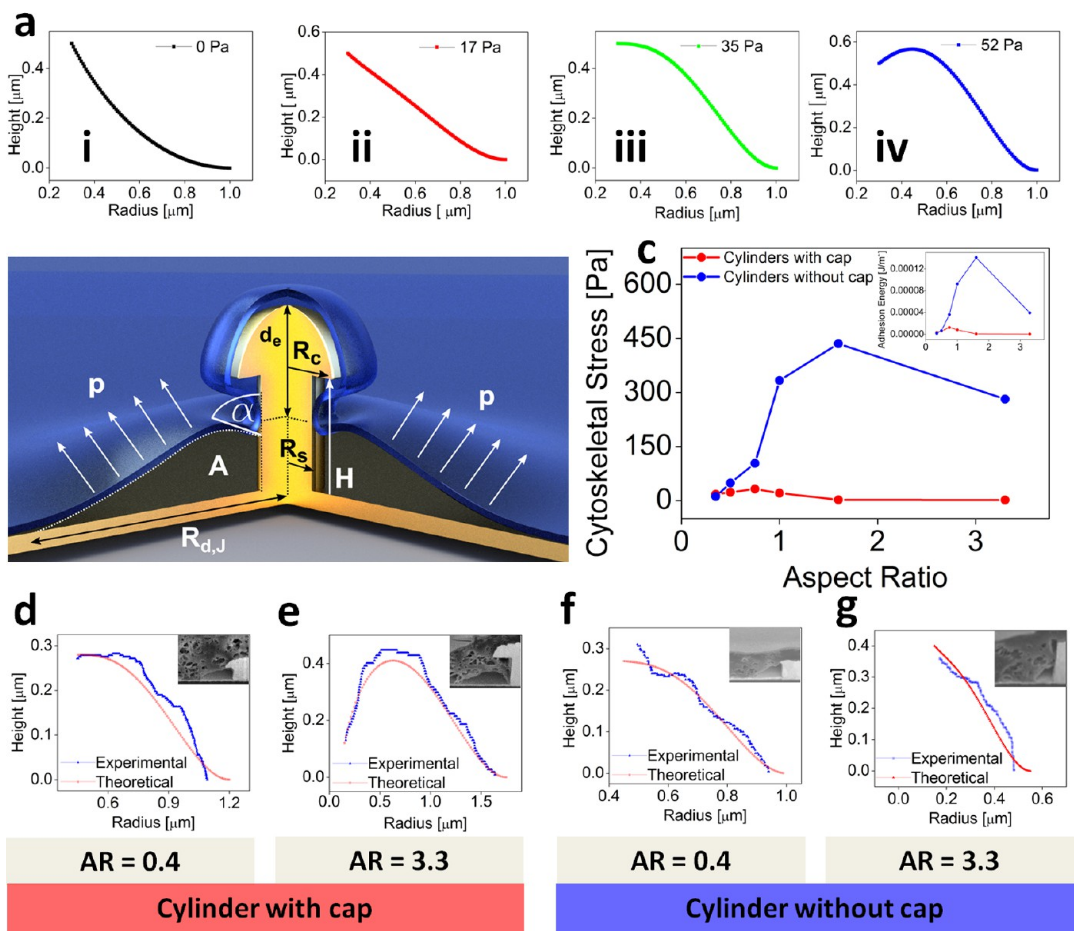

**Figure 6. Theoretical analysis of the membrane deformation profiles in the center of the cell. (a) Membrane deformation for fixed pillar radius, $R_s$, membrane height at the stalk height, $H$, detachment length, $R_{d,F}$, and several values of cytoskeletal stress, $p$. (b) Schematic describing the theoretical model. (c) Cytoskeletal stress and strength of adhesion to the substrate for several aspect ratios, extracted from the experimental data given in Figure 5d−g), comparison of experimental and theoretical deformation profiles.**

and down to $w = 500$ nJ/m$^2$ for cylinders with cap. The values of the adhesion strengths are similar to those that have been measured for adhered vesicles[47] but smaller than those quoted by Xie *et al.*[27]

## CONCLUSION

Previous works regarding in-cell recordings considered the possibility to have a 3D nano- or microelectrode in the very proximity of the cell junctional membrane. This very close contact, confirmed also by TEM studies, improved the electrical seal resistance and, thus, the quality of the recorded action potentials from electrogenic cells. In this work, we have studied the effect of shape and dimensions of 3D nanopillars/nanoelectrodes using a systematic approach for analyzing the cell−nenoelectrode interface. First, we found that HL-1 cells prefer to engulf 3D nanostructures in the center of the cell compared to the periphery. Cells deform their membranes in different ways depending on the position of the engulfment-like event. It is very likely that the engulfed nanopillar is stabilized by an actin network in the center of the cell, while this network is in a much more dynamic state at the edge of the cell, driving the filopodia on the planar substrate. Then, we performed combined experimental and theoretical studies at the periphery of the cell, which allow the prediction of free membrane deformations by considering simple lipid-bilayer deformations. For the center of the cell, we need to additionally account for the contribution of the cytoskeletal stress. Consequently, we can estimate the junctional membrane deformation depending on nanopillar shape and dimensions, assuming that the free membrane cannot sense the 3D nanostructure underneath due to the intervening contents of the cell. We conclude that in both scenarios—edge and center−higher membrane coverage of the 3D electrode is observed for the cylinder with cap. We estimated the effective seal resistance in the vicinity of our nanoelectrode from the SEM images according to the method described by Fendyur *et al.*,[20] assuming a cleft between the adhered cell membrane and nanoelectrode of 25 nm (see Supporting Information S6). In the center of the cell, we obtained seal resistances of about 6 and 54 MΩ for $\gamma$ of 0.4 and 3.3, respectively, for capped cylinders.

These values are similar to those reported before by modeling.[20,24] Beside the shape of the 3D nanostructures, the dependency of the seal resistance on the engulfment-like position suggests that for in-cell recording the position of the cell on the active electrode plays a key role for the quality of the signal. In summary, capped cylinders with $\gamma = 3.3$ energetically and biomechanically favor hourglass-like adhesion compared to nanopillars with smaller $\gamma$. We can conclude that for interfacing electrogenic cells with 3D nanoelectrodes positioned within the cell, the shape and size of the 3D nanoelectrode matter. Future studies shall focus on recordings of electrogenic cells with nanopillars whose caps have been designed on the basis of the results presented here. Furthermore, we will investigate whether neuronal cell membranes respond differently to the HL-1 cells considering that neuronal cells are definitely less stiff than cardiomyocytes-like cells, which are typically as stiff as fibroblasts.

## METHODS

**Chemicals.** Unless otherwise noted, all the chemicals were provided by Sigma-Aldrich GmbH.

**Fabrication of Gold Spines.** Gold 3D nanostructures were fabricated similarly as previously shown.[21] In summary, a layer of evaporated gold of 40 nm was deposited on a 12 × 12 mm$^2$ silicon oxide substrate. To fabricate the 3D nanostructures with different stalk heights, three different electron beam resists have been spin-coated on to the substrates: AR-P 669.04, 679.04, and 669.07 (Allresist GmBH) at 3000 rpm, which resulted in a resist thickness of about 300, 500, and about 1000 nm, respectively. The arrays of circular apertures (300, 500, 800 nm of diameter) were created by means of electron beam lithography with a pitch of 25 $\mu$m. Next, the samples were baked at high temperature in order to form round shaped aperture edges. Subsequently, these apertures were filled with gold by electrodeposition. In the case of the mushroom shaped pillars, the electrodepostion was performed in order to have caps of 300−2000 nm in diameter. As final step, the resist was removed in acetone. The samples were then cleaned in 2-propanol and flowing distilled water for 4 h, sterilized with UV, and coated with fibronectine and 0.02% Bacto Gelatin (Fisher Scientific) for 1 h.

**HL-1 Culture.** Confluent HL-1 cells[48] in a T-25 flask were treated with 0.05% Trypsin/EDTA (Life Technologies), suspended in 5 mL of Claycomb medium and centrifuged for 5 min at 1700 rpm. The cell pellet was resuspended in 5 mL of medium; 15 $\mu$L of the suspension was then plated on every substrate, and after 1 h, the medium volume was filled up to 3 mL for every sample.

**Membrane Stain and Fixation of Cells.** After 2 DIV, the cells were washed with phosphate buffer saline (PBS) solution (137 mM NaCl, 2.7 mM KCl, 8 mM $Na_2HPO_4$, 1.8 mM $KH_2PO_4$), chemically fixed with 3.2% glutaraldehyde in PBS. Cell membranes and nuclei were stained with 1:1000 dilution in PBS of Wheat Germ Agglutinin Alexa Fluor 488 (Life Technologies) and 1:500 in PBS of DAPI. The cells were observed in a fluorescence microscope (AxioImager Z.1, Carl Zeiss AG) and then, prepared for the scanning electron microscope. For the actin stain, the membrane was permeablized with 0.1% TritonX in milk blocking solution, Phalloidin-Biotin-XX (Life Technologies) compound was diluted in a 1:500 concentration in the total volume, and, finally, Streptavidin-Nanogold-AlexaFluor 488 (Life Technologies) was used in a dilution of 1:50 in milk blocking solution. In addition, the samples were stained with 0.5% osmium tetroxide and washed with water. The water was replaced with ethanol in different concentrations (10%−100% v/v), and finally, the cells on the substrates were dried by critical point drying (see Supporting Information S4). Before the SEM, a thin layer of platinum was sputtered on the samples.

**Scanning Electron Microscopy (SEM) and Focused Ion Beam (FIB).** The focused ion beam cross-sectioning was performed with a Helios Nanolab Dual-beam (FEI Company). First, a 0.4 $\mu$m layer of platinum was deposited *via* electron beam induced deposition (EBID). The sample was then tilted by 52° and an additional 0.4 $\mu$m thick platinum layer was deposited by ion beam induced deposition (IBID) with a current of 0.43 nA at 30 kV. The milling and the polishing of the cross sections have been performed using a voltage of 30 kV and a current of 80 pA.[49] The images were then acquired in scanning electron mode fixing a voltage at 3 kV.

**Image Processing and Analysis.** Images were processed and analyzed with ImageJ. The contrast and the brightness were not varied from the original SEM pictures. All the parameters evaluated and discussed in the paper were manually analyzed, except for the membrane profile, in the case of the pillar positioned at the edge of the cell. In this case, an automatic macro utility was used for the outline recognition (courtesy of Zhanna Santybayeva, ICS-7, Forschungszentrum Juelich, Germany). For data analysis and plotting, we used Origin 8.2 (OriginLab).

**Theoretical Model.** The deformation energy cost due to bending energy for a fluid membrane is given by,

$$E_{\mathrm{bend}} = 2\kappa \int_S \mathrm{d}S\, H^2$$

where $\kappa$ is the bending rigidity of the membrane, $H = (c_1 + c_2)/2$ the mean curvature, and $S$ is the entire membrane area. The curvatures $c_1$ and $c_2$ are the principal curvatures, *i.e.*, the smallest and the largest curvature at each point of the membrane. We show that the experimentally measured membrane deformation profiles can be described well even with a vanishing surface tension contribution. The adhesion energy gain is given by the contact energy between the pillar and the nanostructure,

$$E_{\mathrm{ad}} = -w \int_{S_{\mathrm{ad}}} \mathrm{d}S$$

where $w$ is the adhesion strength and $S_{\mathrm{ad}}$ is the membrane area adhered to the structured substrate. For calculating the deformation profile of the lower membrane, we use in addition a homogeneous pressure term, $-ph(x,y)$, where the membrane is described by a height field $h(x,y)$ and the pressure mimics the contractile forces of the cytoskeleton. Assuming a perfect wetting condition, *i.e.*, a contact angle of $\pi$ at the detachment point of the tensionless membrane with either the substrate (for the junctional membrane deformation at center of the cell) or on the junctional membrane (for the free membrane deformation at the edge of the cell), we estimate an effective strength of the adhesion $w$ using the local curvature $c$ at the detachment point such that, $c = (2w/k)^{1/2}$.

*Conflict of Interest:* The authors declare no competing financial interest.

*Supporting Information Available:* Base aspect ratio calculation, FIB image analysis for pillars engulfed in the center of the cell, attachment angle analysis, immune-gold-stain-of actin filaments, analysis of membrane detachment, calculating of effective seal resistances, theoretical analysis for pillars engulfed in the center of the cell, and theoretical analysis for pillars engulfed at the edge of the cell. This material is available free of charge *via* the Internet at http://pubs.acs.org.

*Acknowledgment.* F.S. and S.D. acknowledge the International Helmholtz Research School of Biophysics and Soft Matter

(IHRS BioSoft) for providing a platform to develop this collaborative project. Direct funding to support theoretical work from the EU FP7 NMP collaborative project PreNanoTox (Project Grant 309666, GG) is acknowledged. S.D. thanks Ken Brakke (Selinsgrove, PA) for his assistance and helpful discussions in numerical techniques about Surface Evolver. The authors thank Rudolf Merkel (Jülich), Zhanna Santybayeva (Jülich) and Markus Deserno (Pittsburgh, PA) for stimulating discussions and advice. The authors thank Vanessa Maybeck (Jülich) for helpful discussions and language advice.

## REFERENCES AND NOTES

1. Bakkum, D. J.; Frey, U.; Radivojevic, M.; Russell, T. L.; Müller, J.; Fiscella, M.; Takahashi, H.; Hierlemann, A. Tracking Axonal Action Potential Propagation on a High-Density Microelectrode Array across Hundreds of Sites. *Nat. Commun.* **2013**, *4*, No. 2181.
2. Dagnelie, G. Retinal Implants: Emergence of a Multidisciplinary Field. *Curr. Opin. Neurol.* **2012**, *25*, 67–75.
3. Volkmann, J.; Albanese, A.; Antonini, A.; Chaudhuri, K. R.; Clarke, C. E.; de Bie, R. M. A.; Deuschl, G.; Eggert, K.; Houeto, J.-L.; Kulisevsky, J.; *et al.* Selecting Deep Brain Stimulation or Infusion Therapies in Advanced Parkinson's Disease: An Evidence-Based Review. *J. Neurol.* **2013**, *260*, 2701–2714.
4. Fisher, J. D.; Kim, S. G.; Mercando, A. D. Electrical Devices for Treatment of Arrhythmias. *Am. J. Cardiol.* **1988**, *61*, A45–A57.
5. Spira, M. E.; Hai, A. Multi-Electrode Array Technologies for Neuroscience and Cardiology. *Nat. Nanotechnol.* **2013**, *8*, 83–94.
6. Hai, A.; Shappir, J.; Spira, M. E. In-Cell Recordings by Extracellular Microelectrodes. *Nat. Methods* **2010**, *7*, 200–202.
7. Silva, G. A. Neuroscience Nanotechnology: Progress, Opportunities and Challenges. *Nat. Rev. Neurosci.* **2006**, *7*, 65–74.
8. Almquist, B. D.; Melosh, N. A. Fusion of Biomimetic Stealth Probes into Lipid Bilayer Cores. *Proc. Natl. Acad. Sci. U.S.A.* **2010**, *107*, 5815–5820.
9. Robinson, J. T.; Jorgolli, M.; Shalek, A. K.; Yoon, M.-H.; Gertner, R. S.; Park, H. Vertical Nanowire Electrode Arrays as a Scalable Platform for Intracellular Interfacing to Neuronal Circuits. *Nat. Nanotechnol.* **2012**, *7*, 180–184.
10. Xie, C.; Lin, Z.; Hanson, L.; Cui, Y.; Cui, B. Intracellular Recording of Action Potentials by Nanopillar Electroporation. *Nat. Nanotechnol.* **2012**, *7*, 185–190.
11. Duan, X.; Gao, R.; Xie, P.; Cohen-Karni, T.; Qing, Q.; Choe, H. S.; Tian, B.; Jiang, X.; Lieber, C. M. Intracellular Recordings of Action Potentials by an Extracellular Nanoscale Field-Effect Transistor. *Nat. Nanotechnol.* **2012**, *7*, 174–179.
12. Ross, A. M.; Jiang, Z.; Bastmeyer, M.; Lahann, J. Physical Aspects of Cell Culture Substrates: Topography, Roughness, and Elasticity. *Small* **2012**, *8*, 336–355.
13. Sniadecki, N. J.; Desai, R. A.; Ruiz, S. A.; Chen, C. S. Nanotechnology for Cell−Substrate Interactions. *Ann. Biomed. Eng.* **2006**, *34*, 59–74.
14. Andersson, A.-S.; Bäckhed, F.; von Euler, A.; Richter-Dahlfors, A.; Sutherland, D.; Kasemo, B. Nanoscale Features Influence Epithelial Cell Morphology and Cytokine Production. *Biomaterials* **2003**, *24*, 3427–3436.
15. Pogodin, S.; Hasan, J.; Baulin, V. A.; Webb, H. K.; Truong, V. K.; Phong Nguyen, T. H.; Boshkovikj, V.; Fluke, C. J.; Watson, G. S.; Watson, J. A.; *et al.* Biophysical Model of Bacterial Cell Interactions with Nanopatterned Cicada Wing Surfaces. *Biophys. J.* **2013**, *104*, 835–840.
16. Pierre-Louis, O. Adhesion of Membranes and Filaments on Rippled Surfaces. *Phys. Rev. E: Stat., Nonlinear, Soft Matter Phys.* **2008**, *78*, 021603.
17. Hai, A.; Kamber, D.; Malkinson, G.; Erez, H.; Mazurski, N.; Shappir, J.; Spira, M. E. Changing Gears from Chemical Adhesion of Cells to Flat Substrata toward Engulfment of Micro-Protrusions by Active Mechanisms. *J. Neural Eng.* **2009**, *6*, 066009.
18. Van Meerbergen, B.; Jans, K.; Loo, J.; Reekmans, G.; Braeken, D.; Seon-Ah, C.; Bonroy, K.; Maes, G.; Borghs, G.; Engelborghs, Y.; *et al.* Peptide-Functionalized Microfabricated Structures for Improved on-Chip Neuronal Adhesion. In *2008 30th Annual International Conference of the IEEE Engineering in Medicine and Biology Society*; IEEE: New York, 2008; Vols. 1−8, pp 1833−1836.
19. Xie, C.; Hanson, L.; Xie, W.; Lin, Z.; Cui, B.; Cui, Y. Noninvasive Neuron Pinning with Nanopillar Arrays. *Nano Lett.* **2010**, *10*, 4020–4024.
20. Fendyur, A.; Mazurski, N.; Shappir, J.; Spira, M. E. Formation of Essential Ultrastructural Interface between Cultured Hippocampal Cells and Gold Mushroom-Shaped MEA—Toward "IN-CELL" Recordings from Vertebrate Neurons. *Front. Neuroeng.* **2011**, *4*, No. 14.
21. Panaitov, G.; Thiery, S.; Hofmann, B.; Offenhäusser, A. Fabrication of Gold Micro-Spine Structures for Improvement of Cell/Device Adhesion. *Microelectron. Eng.* **2011**, *88*, 1840–1844.
22. Martiradonna, L.; Quarta, L.; Sileo, L.; Schertel, A.; Maccione, A.; Simi, A.; Dante, S.; Scarpellini, A.; Berdondini, L.; De Vittorio, M. Beam Induced Deposition of 3D Electrodes to Improve Coupling to Cells. *Microelectron. Eng.* **2012**, *97*, 365–368.
23. VanDersarl, J. J.; Xu, A. M.; Melosh, N. A. Nanostraws for Direct Fluidic Intracellular Access. *Nano Lett.* **2012**, *12*, 3881–3886.
24. Hanson, L.; Lin, Z. C.; Xie, C.; Cui, Y.; Cui, B. Characterization of the Cell-Nanopillar Interface by Transmission Electron Microscopy. *Nano Lett.* **2012**, *12*, 5815–5820.
25. Wierzbicki, R.; Købler, C.; Jensen, M. R. B.; Łopacińska, J.; Schmidt, M. S.; Skolimowski, M.; Abeille, F.; Qvortrup, K.; Mølhave, K. Mapping the Complex Morphology of Cell Interactions with Nanowire Substrates Using FIB-SEM. *PLoS One* **2013**, *8*, e53307.
26. Santoro, F.; Schnitker, J.; Panaitov, G.; Offenhäusser, A. On Chip Guidance and Recording of Cardiomyocytes with 3D Mushroom-Shaped Electrodes. *Nano Lett.* **2013**, *13*, 5379–5384.
27. Xie, X.; Xu, A. M.; Angle, M. R.; Tayebi, N.; Verma, P.; Melosh, N. A. Mechanical Model of Vertical Nanowire Cell Penetration. *Nano Lett.* **2013**, *13*, 6002–6008.
28. Hai, A.; Shappir, J.; Spira, M. E. Long-Term, Multisite, Parallel, In-Cell Recording and Stimulation by an Array of Extracellular Microelectrodes. *J. Neurophysiol.* **2010**, *104*, 559–568.
29. Hai, A.; Spira, M. E. On-Chip Electroporation, Membrane Repair Dynamics and Transient in-Cell Recordings by Arrays of Gold Mushroom-Shaped Microelectrodes. *Lab Chip* **2012**, *12*, 2865–2873.
30. Verma, P.; Melosh, N. A. Gigaohm Resistance Membrane Seals with Stealth Probe Electrodes. *Appl. Phys. Lett.* **2010**, *97*, 033704-1–033704-3.
31. Fendyur, A.; Spira, M. E. Toward on-Chip, in-Cell Recordings from Cultured Cardiomyocytes by Arrays of Gold Mushroom-Shaped Microelectrodes. *Front. Neuroeng.* **2012**, *5*, No. 21.
32. Braeken, D.; Huys, R.; Jans, D.; Loo, J.; Rand, D. R.; Borghs, G.; Callewaert, G.; Bartic, C. Local Electrical Stimulation of Single Myocytes Using Three-Dimensional Electrode Arrays with Small Interelectrode Distances. In *World Congress on Medical Physics and Biomedical Engineering, September 7−12, 2009, Munich, Germany*; Dössel, O., Schlegel, W. C., Eds.; IFMBE Proceedings; Springer: Berlin Heidelberg, 2010; pp 212−215.
33. Spira, M. E.; Kamber, D.; Dormann, A.; Cohen, A.; Bartic, C.; Borghs, G.; Langedijk, J. P. M.; Yitzchaik, S.; Shabthai, K.; Shappir, J. Improved Neuronal Adhesion to the Surface of Electronic Device by Engulfment of Protruding Micro-Nails Fabricated on the Chip Surface. In *Solid-State Sensors, Actuators and Microsystems Conference, 2007. TRANSDUCERS 2007. International*; IEEE: New York, 2007; pp 1247−1250.
34. Kaksonen, M.; Toret, C. P.; Drubin, D. G. Harnessing Actin Dynamics for Clathrin-Mediated Endocytosis. *Nat. Rev. Mol. Cell Biol.* **2006**, *7*, 404–414.
35. Lamaze, C.; Fujimoto, L. M.; Yin, H. L.; Schmid, S. L. The Actin Cytoskeleton Is Required for Receptor-Mediated Endocytosis

in Mammalian Cells. *J. Biol. Chem.* **1997**, *272*, 20332–20335.

36. Jeng, R. L.; Welch, M. D. Cytoskeleton: Actin and Endocytosis—No Longer the Weakest Link. *Curr. Biol.* **2001**, *11*, R691–R694.
37. Claycomb, W. C.; Lanson, N. A.; Stallworth, B. S.; Egeland, D. B.; Delcarpio, J. B.; Bahinski, A.; Izzo, N. J. HL-1 Cells: A Cardiac Muscle Cell Line That Contracts and Retains Phenotypic Characteristics of the Adult Cardiomyocyte. *Proc. Natl. Acad. Sci. U.S.A.* **1998**, *95*, 2979–2984.
38. Dasgupta, S.; Auth, T.; Gompper, G. Wrapping of Ellipsoidal Nano-Particles by Fluid Membranes. *Soft Matter* **2013**, *9*, 5473–5482.
39. Dasgupta, S.; Auth, T.; Gompper, G. Shape and Orientation Matter for the Cellular Uptake of Nonspherical Particles. *Nano Lett.* **2014**, *14*, 687–693.
40. Fromherz, P.; Offenhausser, A.; Vetter, T.; Weis, J. A Neuron-Silicon Junction: A Retzius Cell of the Leech on an Insulated-Gate Field-Effect Transistor. *Science* **1991**, *252*, 1290–1293.
41. Vinzenz, M.; Nemethova, M.; Schur, F.; Mueller, J.; Narita, A.; Urban, E.; Winkler, C.; Schmeiser, C.; Koestler, S. A.; Rottner, K.; *et al.* Actin Branching in the Initiation and Maintenance of Lamellipodia. *J. Cell Sci.* **2012**, *125*, 2775–2785.
42. Helfrich, W. Elastic Properties of Lipid Bilayers: Theory and Possible Experiments. *Z. Naturforsch., C: Biochem., Biophys., Biol., Virol.* **1973**, *28*, 693–703.
43. Noguchi, H.; Gompper, G. Shape Transitions of Fluid Vesicles and Red Blood Cells in Capillary Flows. *Proc. Natl. Acad. Sci. U.S.A.* **2005**, *102*, 14159–14164.
44. Sileo, L.; Pisanello, F.; Quarta, L.; Maccione, A.; Simi, A.; Berdondini, L.; De Vittorio, M.; Martiradonna, L. Electrical Coupling of Mammalian Neurons to Microelectrodes with 3D Nanoprotrusions. *Microelectron. Eng.* **2013**, *111*, 384–390.
45. Ananthakrishnan, R.; Ehrlicher, A. The Forces behind Cell Movement. *Int. J. Biol. Sci.* **2007**, *3*, 303–317.
46. Thomas, W. E.; Vogel, V.; Sokurenko, E. Biophysics of Catch Bonds. *Annu. Rev. Biophys.* **2008**, *37*, 399–416.
47. Smith, A.-S.; Seifert, U. Effective Adhesion Strength of Specifically Bound Vesicles. *Phys. Rev. E* **2005**, *71*, 061902.
48. Hai, A.; Dormann, A.; Shappir, J.; Yitzchaik, S.; Bartic, C.; Borghs, G.; Langedijk, J. P. M.; Spira, M. E. Spine-Shaped Gold Protrusions Improve the Adherence and Electrical Coupling of Neurons with the Surface of Micro-Electronic Devices. *J. R. Soc., Interface* **2009**, *6*, 1153–1165.
49. Claycomb, W. C.; Lanson, N. A.; Stallworth, B. S.; Egeland, D. B.; Delcarpio, J. B.; Bahinski, A.; Izzo, N. J. HL-1 Cells: A Cardiac Muscle Cell Line That Contracts and Retains Phenotypic Characteristics of the Adult Cardiomyocyte. *Proc. Natl. Acad. Sci. U.S.A.* **1998**, *95*, 2979–2984.
50. Santoro, F.; Neumann, E.; Panaitov, G.; Offenhäusser, A. FIB Section of Cell−Electrode Interface: An Approach for Reducing Curtaining Effects. *Microelectron. Eng.* **2014**, *124*, 17–21.